

Universal routing of light via optical thermodynamics

In the format provided by the
authors and unedited

Table of Contents

Supplementary Note I: Experimental setup	2
Supplementary Note II: Generation of optical mesh lattices	3
Supplementary Note III: Mode calculation.....	4
Supplementary Note IV: Mesh lattice model to the continuous Schrödinger equation.....	6
Supplementary Note V: Calculation of modal occupancy and kinetic energy	7
Supplementary Note VI: Additional experimental results.....	8
Supplementary Note VII: Multiple excitation protocol	10
Supplementary Note VIII: Pulse dynamics in a weak linear potential	11
Supplementary Note IX: The effect of input port variation.....	12
Supplementary Note X: The effect of input power and potential slope	14
Supplementary Note XI: The effect of input phase difference	15
Supplementary Note XII: Time-reversal symmetry	16
Supplementary Note XIII: Derivation of Thermodynamic Variables	18
Supplementary References.....	20

Supplementary Note I: Experimental setup

The experimental platform consists of a pulse generation block, followed by the two coupled fiber loops (see Fig. S1). In the pulse generation part, denoted as the seed pulse module (SPM), a 20 ns rectangular-shaped pulse is cut out of the CW signal of a high-coherent DFB laser (carrier wavelength $\lambda = 1550$ nm) by using a Mach-Zehnder modulator (MZM). The generated pulse is then amplified by a subsequent erbium-doped fiber amplifier (EDFA) to achieve the desired nonlinear self-phase shift in the experiment. A tunable optical bandpass filter (BPF) is used thereafter to spectrally purify the pulse by eliminating out-of-band amplified spontaneous emission (ASE) from the amplifier. Finally, the peak power of the pulse is precisely adjusted using a variable optical attenuator (VOA) before being injected into the loop u through an optical switch, functioning as a gate.

The main part of the experimental setup (see Fig. S1) consists of two dispersion-compensating fiber (DCF, type: OFS-SMF-DK) loops with an average length of 3 km and nonlinear coefficient of $\gamma \approx 7.5$ (W. km) $^{-1}$ [1, 2], connected by a central 50/50 coupler. Each loop contains an electro-optic phase modulator to impose phase shifts $\phi(n, m)$, creating an effective position-dependent refractive index distribution (potential) in the temporal photonic lattice [3]. Moreover, EDFAs are used in each loop to compensate for all the insertion losses to ensure power conservation. The EDFAs are optically gain-clamped using a CW pilot laser operating at a blue-shifted wavelength of $\lambda = 1534$ nm, which is coupled to the amplifiers via wavelength division multiplexers (WDM) and subsequently removed by tunable BPFs positioned immediately after the amplifiers. To align the signal's polarization for controlling pulse interference and ensuring proper operation of all polarization-sensitive components (e.g., the EDFAs and PMs), mechanical polarization controllers (PCs), indicated by three black circles, are used. The polarization state is continuously monitored by photodetectors coupled through polarizing beam splitters (PBS). The pulse energies are measured with a photodetector (PD) and mapped onto the synthetic lattice based on their arrival time at the detector.

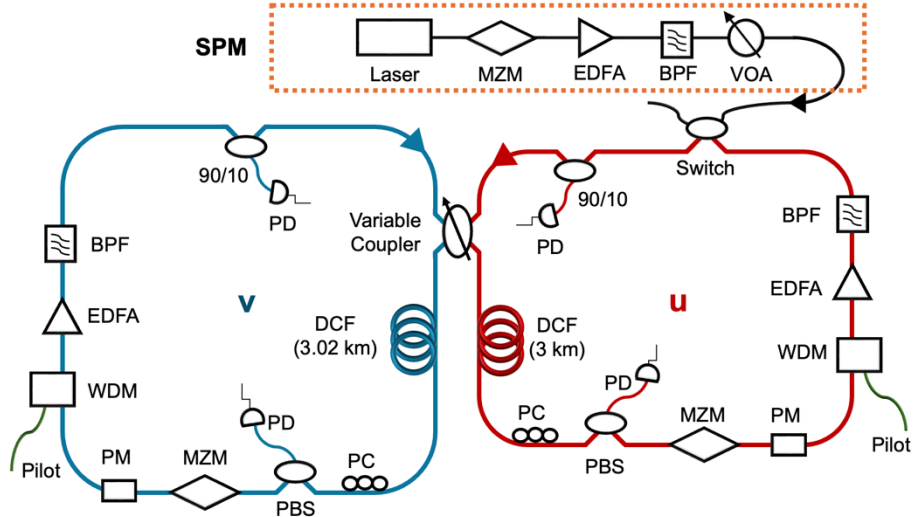


Figure S1: Experimental setup. The sketch of the experimental setup consists of a pulse generation block (SPM: seed pulse module) and coupled fiber loops connected via a variable coupler. The pulse intensities are monitored by photodetectors (PD) connected through couplers with a fixed 90/10 coupling ratio. MZM: Mach-Zehnder modulator; EDFA: erbium-doped fiber amplifier; BPF: bandpass filter; VOA: variable optical attenuator; DCF: dispersion-compensating fiber; PC: polarization controller; PBS: polarizing beam splitter; PM: phase modulator; WDM: wavelength division multiplexer.

Supplementary Note II: Generation of optical mesh lattices

Due to the slight length difference between the two loops ($\Delta L \approx 20$ m), a pulse sequence passing through the short (u) and long (v) loops is advanced or delayed by $\Delta t \approx 50$ ns in the time domain. In this context, following the concept of tailoring synthetic dimensions using a time-multiplexing technique [4], the discrete arrival times correspond to positions $n - 1$ or $n + 1$ in the effective spatial domain, respectively (see Fig. S2 (a)). After a mean roundtrip time $\bar{T} \approx 15 \mu\text{s}$, the pulse sequences are recombined in the 50/50 coupler, and m increases by +1. Thus, the whole system resembles the light dynamics in a waveguide array with lumped coupling and is modeled by the following set of discrete equations:

$$\begin{aligned} u_n^{m+1} &= (t_{n+1}^m u_{n+1}^m + i r_{n+1}^m v_{n+1}^m) e^{i\Gamma |t_{n+1}^m u_{n+1}^m + i r_{n+1}^m v_{n+1}^m|^2} e^{i\phi(n,m)} \\ v_n^{m+1} &= (t_{n-1}^m v_{n-1}^m + i r_{n-1}^m u_{n-1}^m) e^{i\Gamma |t_{n-1}^m v_{n-1}^m + i r_{n-1}^m u_{n-1}^m|^2} e^{i\phi(n,m)} \end{aligned} \quad (\text{S1})$$

where u_n^m and v_n^m represent the complex amplitudes of the pulses in loop u and v , respectively, at time step m and lattice position n . In this description, t_n^m and r_n^m are the transmission and reflection coefficients of the optical coupler ($t^2 + r^2 = 1$), $\phi(n, m)$ is an external phase modulation, and Γ denotes the nonlinearity coefficient of the system, which defines the strength of the nonlinear phase accumulation experienced by pulses in proportion to their power [2]. In our setup, a nonlinear phase shift of 0.5π is accumulated when a peak power of about ~ 120 mW is injected.

In the linear regime and in the absence of any external phase modulation, a single injection pulse spreads ballistically, with its peak power traveling away from the center of the lattice. This so-called classical light walk, depicted in Fig. S2 (b), can be considerably modified in the presence of phase modulation [5] or nonlinearity [6, 7].

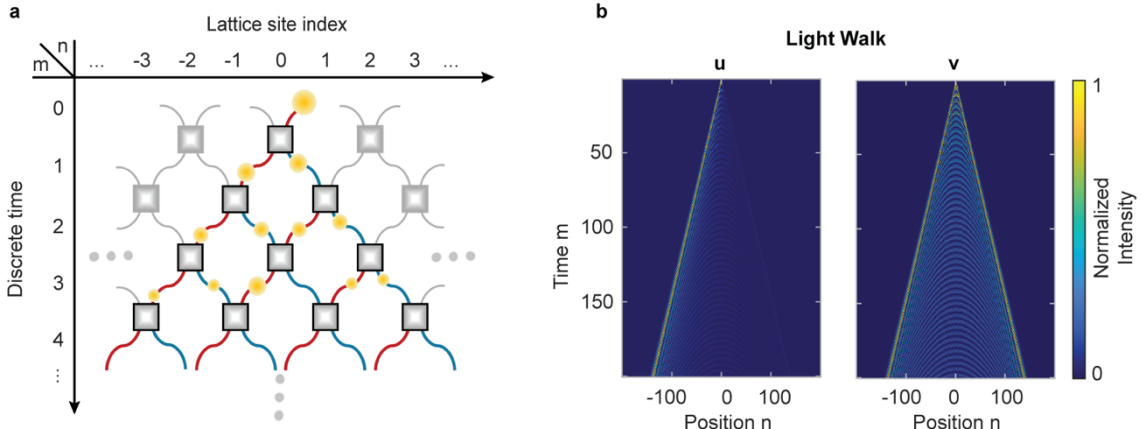


Figure S2: Wave dynamics in time synthetic photonic mesh lattices. (a) Introducing an imbalance in path lengths between the two fiber loops causes the initial pulse (marked by the yellow circle) to reach the coupler at different times. Therefore, a roundtrip in the short (red) and long (blue) loops corresponds to motion to the left and right, respectively. This creates a 1+1D lattice, which is spanned by the discrete time m and discrete position n . During each roundtrip m , arriving pulses are sampled electronically and mapped onto the lattice sites based on their arrival time at the photodetectors. (b) The evolution of pulse dynamics in the short (u) and long (v) loops within a homogeneous lattice ($\phi = 0$ and 50/50 coupler) upon injection of a laser pulse into the short loop.

Supplementary Note III: Mode calculation

By truncating the mesh lattice in time to a finite number of positions and, therefore, limiting the system to a finite number of modes, we impose the phase potential depicted in Fig. S3 (b) and calculate the eigenvalues of the system. We then link Eq. (S1) to the discrete nonlinear equation presented in the main manuscript, showing that both systems exhibit the same quasi-linear spectrum, with the lowest-order eigenmodes localized at the center of the lattice. Here, we also consider a double-sided triangular-shaped potential (Fig. S3(b)), demonstrating that it retains the key characteristics and localization properties of the potential with an abrupt drop at the position $n = 0$.

The system achieves a finite number of modes by truncating the mesh lattice in Eq. (S1) at specific reflective boundaries ($t_{n=-N} = t_{n=N} = 0$ and $r_{n=-N} = r_{n=N} = 1$), with the lattice size of $4N + 2$. Since the photonic mesh lattices exhibit a periodic unit cell with a periodicity of two in both spatial and temporal domains, in a truncated lattice, a full period of mode evolution requires two roundtrips. As a result, the field evolution from time step m to $m + 2$ can be expressed as follows:

$$|\Psi^{m+2}\rangle = \hat{M}|\Psi^m\rangle \quad (\text{S2})$$

where $|\Psi^m\rangle$ is composed of complex vector amplitude distribution in both loops at time step m (i.e., $|\Psi^m\rangle = [|u^m\rangle; |v^m\rangle] = [u_{n=-N}^m, \dots, u_{n=N}^m, v_{n=-N}^m, \dots, v_{n=N}^m]^T$), and \hat{M} is a unitary evolution operator [8] related to the system's Hermitian Hamiltonian \hat{H} via $\hat{M} = \exp(i\hat{H})$. Altogether, the spectrum of a given lattice configuration can be calculated by:

$$[|\Psi_k\rangle, e^{-i\varepsilon_k}] = \text{eig}(\hat{M}). \quad (\text{S3})$$

In this expression, $|\Psi_k\rangle = [|U\rangle_k; |V\rangle_k]$ denotes the eigenstate of mode k , where the system supports a total of $2N + 2$ modes. The corresponding propagation constant of mode k is given by ε_k .

Figure S3 (c) shows the quasi-linear distribution of the normalized eigenvalues (ε_k), where the mode associated with the largest eigenvalue is identified as the system's fundamental mode, localized at the center of the lattice (see Fig. S3 (a)). Conversely, the mode with the lowest eigenvalue is designated as the highest-order mode, being confined at the edge of the lattice (see Fig. S3 (d)). Additionally, Fig. S3 (a) also depicts mode number 10 spans nearly all lattice positions. It should be noted that, for a better illustration of the eigenmodes, the vectors $|U\rangle_k$ and $|V\rangle_k$ are rearranged based on the field evolution map on the setup (i.e., $[U_k^{(n=-N)}, V_k^{(n=-N)}, \dots, U_k^{(n=N)}, V_k^{(n=N)}]$).

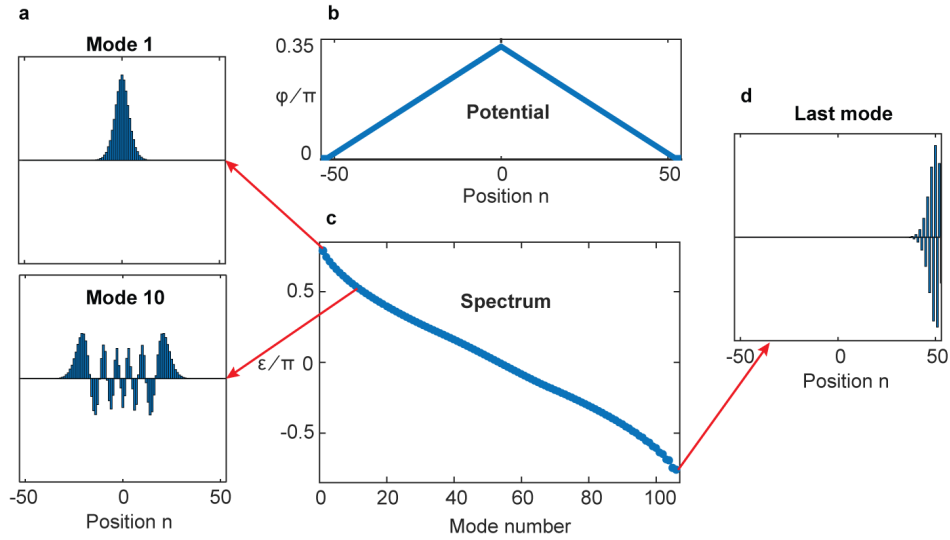


Figure S3: Designed lattice's spectrum. (a) Fundamental mode and 10th mode of the (b) triangular-shaped potential. The fundamental mode is confined at the center of the lattice, associated with the largest eigenvalue, while the higher-order modes spread across the lattice. (c) The quasi-linear eigenvalue spectrum of this model with truncated boundaries. (d) The highest-order mode with the lowest eigenvalue is confined at the edge of the potential.

Supplementary Note IV: Mesh lattice model to the continuous Schrödinger equation

To connect the discrete model in Eq. (S1) with the continuous Schrödinger equation, we use the eigenvalue equation of the system. Given that the periodicity of the mesh lattice is two in both spatial and temporal domains, the pseudo-spinors of our system $\Psi_n^m = [u_n^m, v_n^m]$, in the absence of any phase modulation (i.e., $\phi = 0$), can be expressed as eigenstates (U, V) using the Floquet-Bloch ansatz:

$$\Psi_n^m = [U, V] e^{i(Qn+\theta m)/2} \quad (\text{S4})$$

where θ is the propagation constant and Q is the Bloch momentum. Substituting Eq. (S4) into the double time-step evolution equations (Eq. (S1)) when the transmission coefficient is 50/50, yields the dispersion relation

$$\theta = \pm \cos^{-1} \left(\frac{\cos Q - 1}{2} \right) \quad (\text{S5})$$

Since the excitation is near $Q \sim 0$, the band structure can be expanded up to the second order.

$$\theta \approx \pm \cos^{-1} \left(-\frac{Q^2}{4} \right) \approx \pm \left(\frac{\pi}{2} + \frac{Q^2}{4} \right) \quad (\text{S6})$$

Assuming that variations between consecutive roundtrips are small, we now treat m and n as continuous quasi-time and quasi-space, respectively.

$$i2 \frac{\partial}{\partial t} = \frac{\pi}{2} - \frac{\partial^2}{\partial x^2} \rightarrow i \frac{\partial}{\partial t} \Psi = \left(\frac{\pi}{4} - \frac{1}{2} \frac{\partial^2}{\partial x^2} \right) \Psi \quad (\text{S7})$$

Supplementary Note V: Calculation of modal occupancy and kinetic energy

The modal occupancy of mode k at each time step m , $|c_k(m)|^2$ can be determined by taking the scalar product of the conjugate transpose of the mode field $\langle \Psi_k |$ with the complex amplitude distribution $|\Psi^m\rangle$ in both loops at the time step m (see Suppl. Note III), expressed as:

$$|c_k(m)|^2 = |\langle \Psi_k | \Psi^m \rangle|^2 \quad (\text{S8})$$

In general, the field amplitudes can be expressed through the system's linear eigenstates, i.e., $|\Psi^m\rangle = \sum_{k=1}^M c_k |\Psi_k\rangle$, where M represents the total number of modes. Furthermore, keeping in mind that $\hat{H}|\Psi_k\rangle = \varepsilon_k |\Psi_k\rangle$, the kinetic (internal) energy of our system can be calculated as:

$$U = \langle \Psi^m | \hat{H} | \Psi^m \rangle = \sum_{k=1}^M \varepsilon_k |c_k|^2 \quad (\text{S9})$$

Figure S4 (a) depicts the simulation results of the routing of light in the truncated mesh lattice. The extended propagation time confirms the stability of this behavior and the reduction of microcanonical fluctuations. The increase in optical kinetic energy $|U|$ (Fig. S4 (b)) shifts the modal amplitude $|c_k|^2$ from a superposition of multiple higher-order modes to the fundamental mode at the center of the lattice, as shown in Fig. S4 (c). Figure S4 (d) illustrates averaged modal occupancy in the equilibrium domain fitted to the predicted Rayleigh-Jeans (RJ) distribution associated with power P and mean equilibrium value of kinetic energy U .

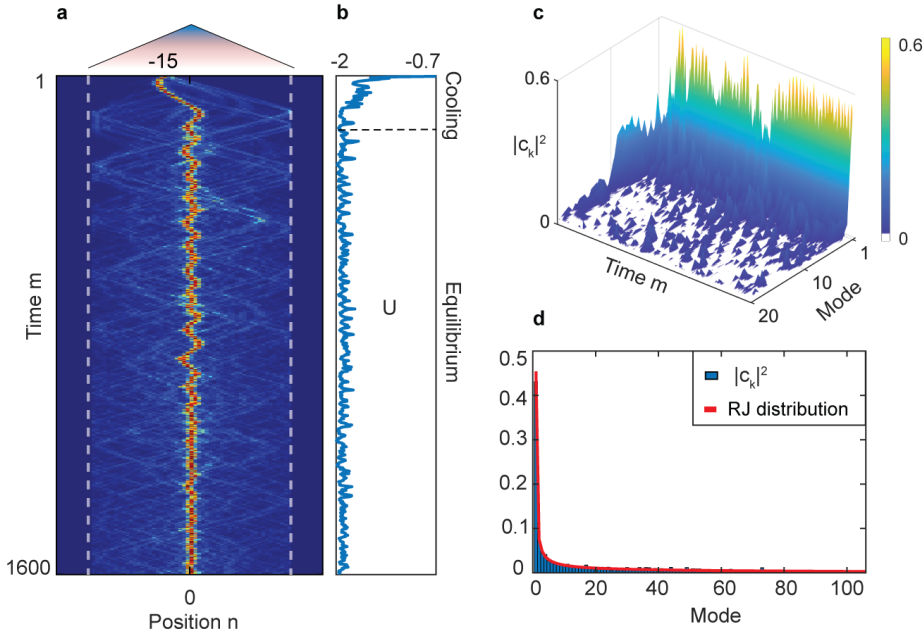


Figure S4: Routing of light in the truncated mesh lattice. (a) Simulation results of the light funneling in the truncated mesh lattice. (b) The calculated optical kinetic energy U , highlighting the regions of optical cooling and equilibrium. (c) Evolution of modal occupancy $|c_k|^2$ at each time step. (d) The time-averaged modal amplitudes are fitted to the theoretical Rayleigh-Jeans distribution, calculated using the mean equilibrium value of U (red continuous line).

Supplementary Note VI: Additional experimental results

To demonstrate the universality of the routing process, we extend our investigation to encompass multiple simultaneous injection points. To this end, we extend the triangular potential by appending its horizontally flipped image while retaining the same $\delta\phi$ as the configuration depicted in the main text (see Fig. 2a). The measurements were performed by considering 4 different scenarios with distinct injection points in both short (u) and long (v) loops. Figures S5 (a) and (b) present the first experimental results, illustrating the non-linear evolution when the injection points are positioned in opposite regions. In the case of symmetric injections (Fig. S5 (a)), the lattice is excited at positions $n = -10$ and $n = 10$ of the short (u) and long (v) loops, respectively. When the two injections are mutually coherent, the fields accumulate the same phase during propagation and constructively interfere when they meet at the funneling path. Nonetheless, the mutual coherence properties are inconsequential to the effectiveness of the process itself, as demonstrated by the non-symmetric injection case in Fig. S5 (b), further reinforcing the claim of a truly conservative funnel for light. Finally, we examine the routing process when the two injection points are placed within the same region of the triangular potential. In Fig. S5 (c), the initial positions are set at $n = -20$ and $n = -10$, of the short (u) and long (v) loops, respectively. The results provide further evidence for the funneling response, showing that the impact of interference between the two incoherent paths remains negligible. In the last example of Fig. S5 (d), a triple excitation case was experimentally put to the test, where light was injected simultaneously at lattice positions $n = -30$, $n = -10$ of the short (u) loop, and at position $n = 10$ of the long (v) loop with equal power.

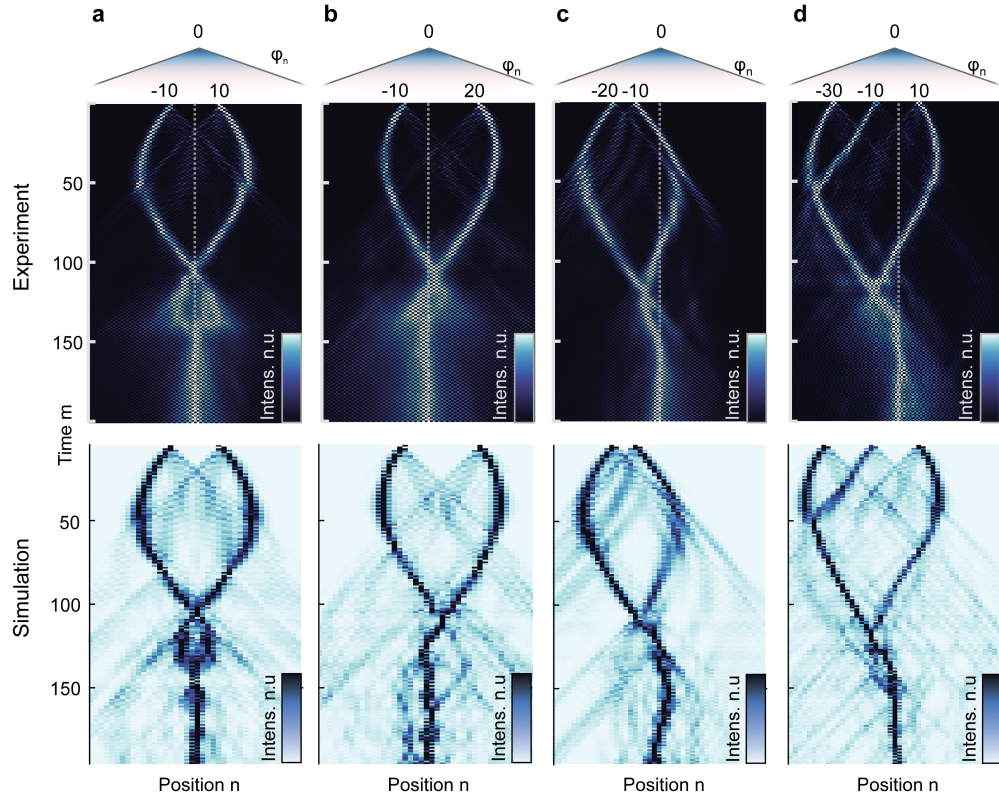


Figure S5: Experimental results investigating the universality of the funneling effect. (a) Double injection result where the lattice is excited at $n = -10$ and $n = 10$ of the short (u) and long (v) loops, respectively. In this symmetric injection scenario, two sources accumulate the same phase by alternating between both loops during propagation, coherently converging toward the center of the lattice. (b) Antisymmetric injection scenario, where the excitation position in the v loop is shifted further from the center of the lattice to $n = 20$, while the left-side injection position remains unchanged. (c) Examining the impact of crosstalk on the funneling effect when two injection sources are excited in close proximity, at $n = -20$ and $n = -10$ of the u and v loops, respectively. (d) Light evolution in triple injection scenario, with excitation positions at $n = -30$ and $n = -10$ of the u loop, and $n = 10$ of the v loop.

Supplementary Note VII: Multiple excitation protocol

At first glance, it seems reasonable to generate a chain of pulses with variable spacing between them, equal to $(n_{i+1} - n_i)\Delta t$, where n_i represents the injection position, and then inject them into the loops. However, the pulse distance within the chain must precisely match the step size Δt . Any inaccuracy over the long propagation distance could disrupt interferometric stabilization, as pulses may interfere even if they haven't propagated through the same number of roundtrips. To address this issue in the experiment, the initial injection state is prepared within the coupled fiber loop using a variable coupler (VC). Figure S6 demonstrates the generation of double and triple pulse injections from a single initial laser pulse injected into the short loop u . For the double injection, VC splits the initial pulse into two at time step $m = 1$ (see Fig. S6 (a)). Afterward, it enables them to circulate in each loop without interference by setting the coupling ratio to 0/100 until they reach the desired distance relative to each other. From this point forward, the phase modulators (PMs) are continuously activated to implement the funneling potential.

A similar process is employed to generate a triple injection from a single pulse as well. At time step $m = 1$, the injected pulse splits into two, with the pulse in the long loop v having double the amplitude of the pulse in the short loop u (see Fig. S6 (b)). After 9 roundtrips of circulation without interference, only the pulse in loop v encounters the 50/50 coupler. The three generated pulses, each with equal power, are now kept circulating for an additional 9 roundtrips to reach the desired special position before PMs are switched on. The coupling ratio and modulation timings used to generate these injection cases are also illustrated in Fig. S6 (a) and (b). It is important to note that in the experimental data obtained using double injection, the two pulses are phase-corrected with respect to each other at the final time step before the phase potential is applied.

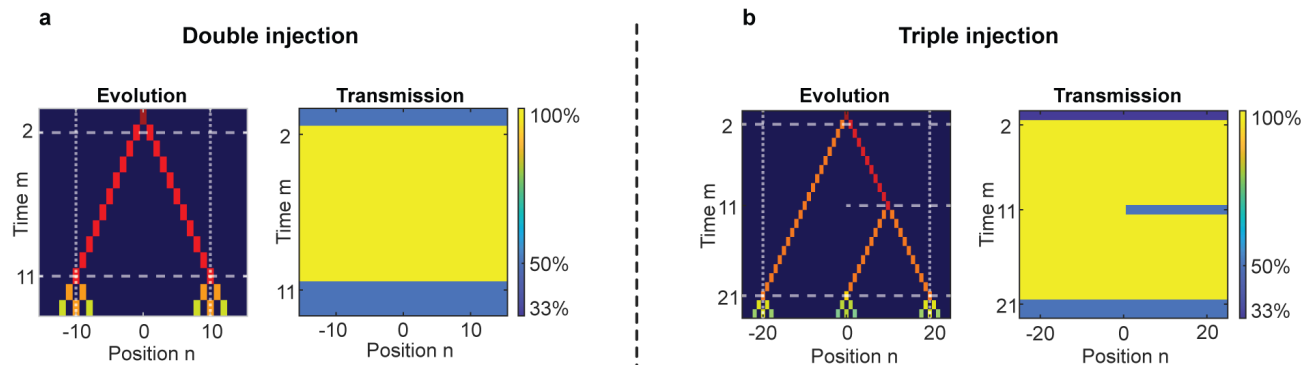


Figure S6: Generation of double and triple pulse injections within the fiber loops. (a) Double pulse injection with equal power is achieved using a variable coupler with the transmission coefficient modulated between 50% and 100% for pulses in both loops. (b) The triple injection is generated by switching the coupler transmission from 33% to 100%. The 50% coupling ratio at time $m = 11$ only acts on a pulse in loop v .

Supplementary Note VIII: Pulse dynamics in a weak linear potential

In the funneling regime, the Hamiltonian energy of light is progressively transferred from the interaction to the kinetic component, facilitating cooling towards the lower-order modes of the lattice, localized at regions of higher local potential values. This process is more clearly observed during evolution in a weakly linear potential without a peak, as illustrated in Fig. S7 (a). The parameters are set at $\delta\Delta = 0.0425$ and $P = 4.1$, well within the optimal regime. After injecting light from a single site, the pulse begins to spread (Fig. S7 (b)). This effect is accurately captured by the second moment of the pulse profile shown in Fig. S7 (c). The behavior in Fig. S7 (b) reveals a close correspondence with the interaction Hamiltonian energy H_{NL} , as depicted in Fig. S7 (d), which gradually decreases to values very close to zero. In other words, the nonlinear nature of the process promotes an all-optical Joules-Thomson expansion where the drop of H_{NL} is primarily due to beam spreading and facilitates optical cooling through a proportionate change of the kinetic energy of light. For timescales that extend beyond the visualization scale of Fig. S7 (a), light begins to evolve quasilinearly, and funneling ceases to be effective. Thus, to observe funneling, it is essential to place the potential peak at an optimal position, allowing the pulse to be effectively captured by the system's lower-order modes.

Figure S7 also reveals a secondary effect that significantly influences the overall efficiency of power funneling. In the funneling regime, the dispersive spreading of the wave packet induces a radiation-like effect that sheds power away from the pulse peak, expediting the cooling process but reducing efficiency. Nonetheless, the cooling primarily relies on the expansion effect, which is mostly responsible for the energy exchange between the two Hamiltonian components.

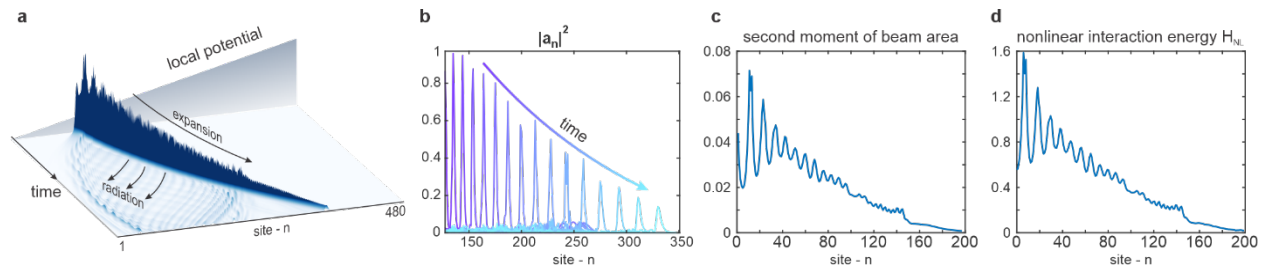


Figure S7: Pulse dynamics in a weak linear potential. (a) Light propagation in a 1D array with a triangular potential. (b) The pulse, captured at various time steps, propagates progressively towards the right, climbing the lattice potential while exhibiting nonlinear spreading. (c) The second moment of the pulse profile. (d) Nonlinear (interaction) Hamiltonian energy.

Supplementary Note IX: The effect of input port variation

Here, we present additional simulation results (Fig. S8) illustrating light routing across various input port scenarios, using the same lattice design ($\delta\Delta = 0.045$) and an input power level of $P = 4.1$ in all cases. As can be seen, channeling the optical energy into the central port of the array in a faithful manner is possible, irrespective of the initial excitation position. Furthermore, Fig. S8 depicts the calculated efficiency of universal routing as a function of the array's potential slope and input power for three selected injection sites (16, 22, and 30), with a red circle indicating the funneling regime. As Fig. S8 suggests, the funneling regime does not critically depend on the specific input conditions, an aspect matching the results depicted in Fig. 4b.

However, the efficiency of the process is primarily limited by energy shedding caused by Peierls-Nabarro effects. As the light packet initially propagates through the lattice, during the first stage of the funneling process, it radiates some of its energy before reaching its final destination, where it thermalizes. As a result, its efficiency does depend on how far the input excitation site is from the funneling port. This becomes evident in Fig. S9 (a), which showcases the funneling efficiency as a function of the distance from the funneling site. Evidently, the efficiency is higher as this distance decreases. As shown in Fig. S9 (a), the efficiency can increase up to 80% when the injection site moves closer to the potential peak. Another aspect that tends to reduce the funneling efficiency has to do with the time-synthetic lattice itself that, by nature, exacerbates the Peierls-Nabarro radiation. This is quite expected given that the lattice is of a Floquet type (time breathing). A similar trend is observed in double-input configurations, where Fig. S9 (b) illustrates how efficiency varies as the spacing between two input sites increases.

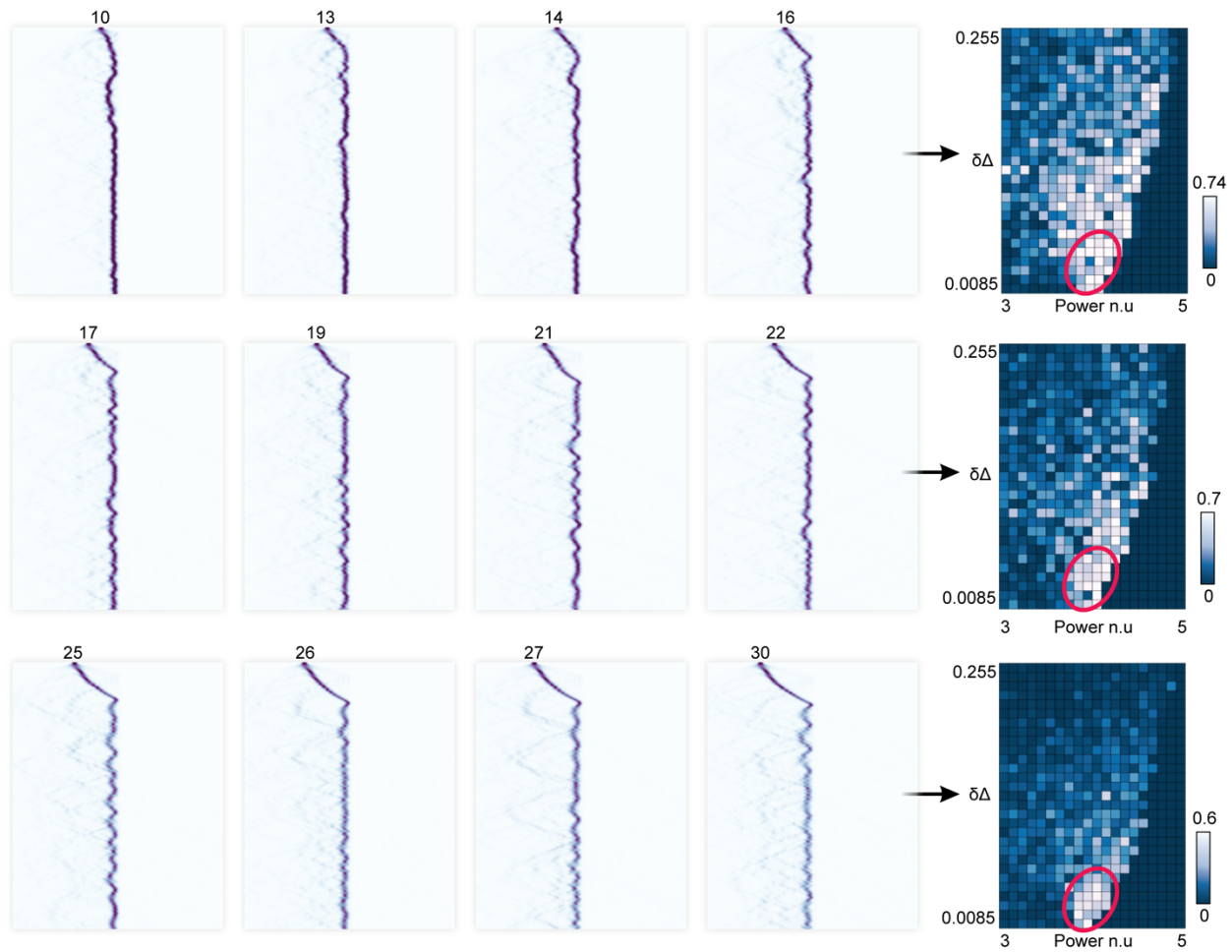


Figure S8: Routing of light across various input ports and calculated funneling region for three different input sites (16, 22, and 30). In all cases, the lattice is designed with a potential slope $\delta\Delta = 0.045$, and light is injected through single ports with normalized power $P = 4.1$.

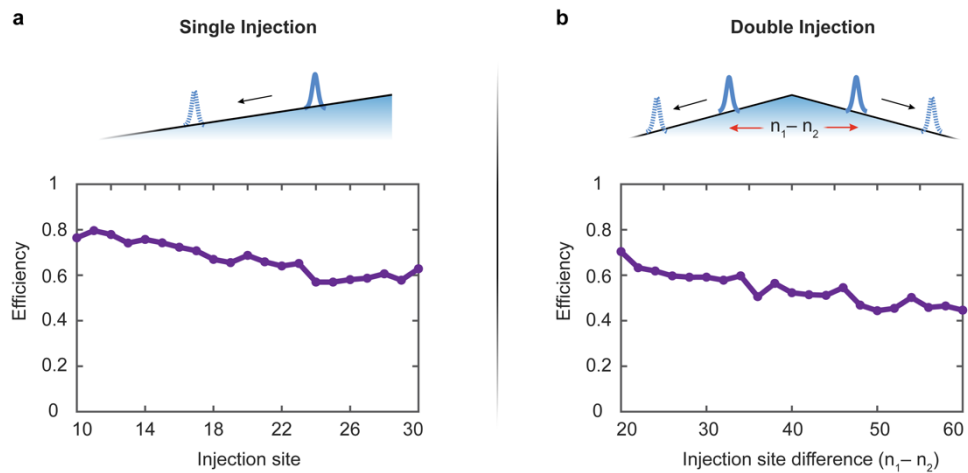


Figure S9: Funneling efficiency as a function of excitation sites for (a) the single injection and (b) the double injection.

Supplementary Note X: The effect of input power and potential slope

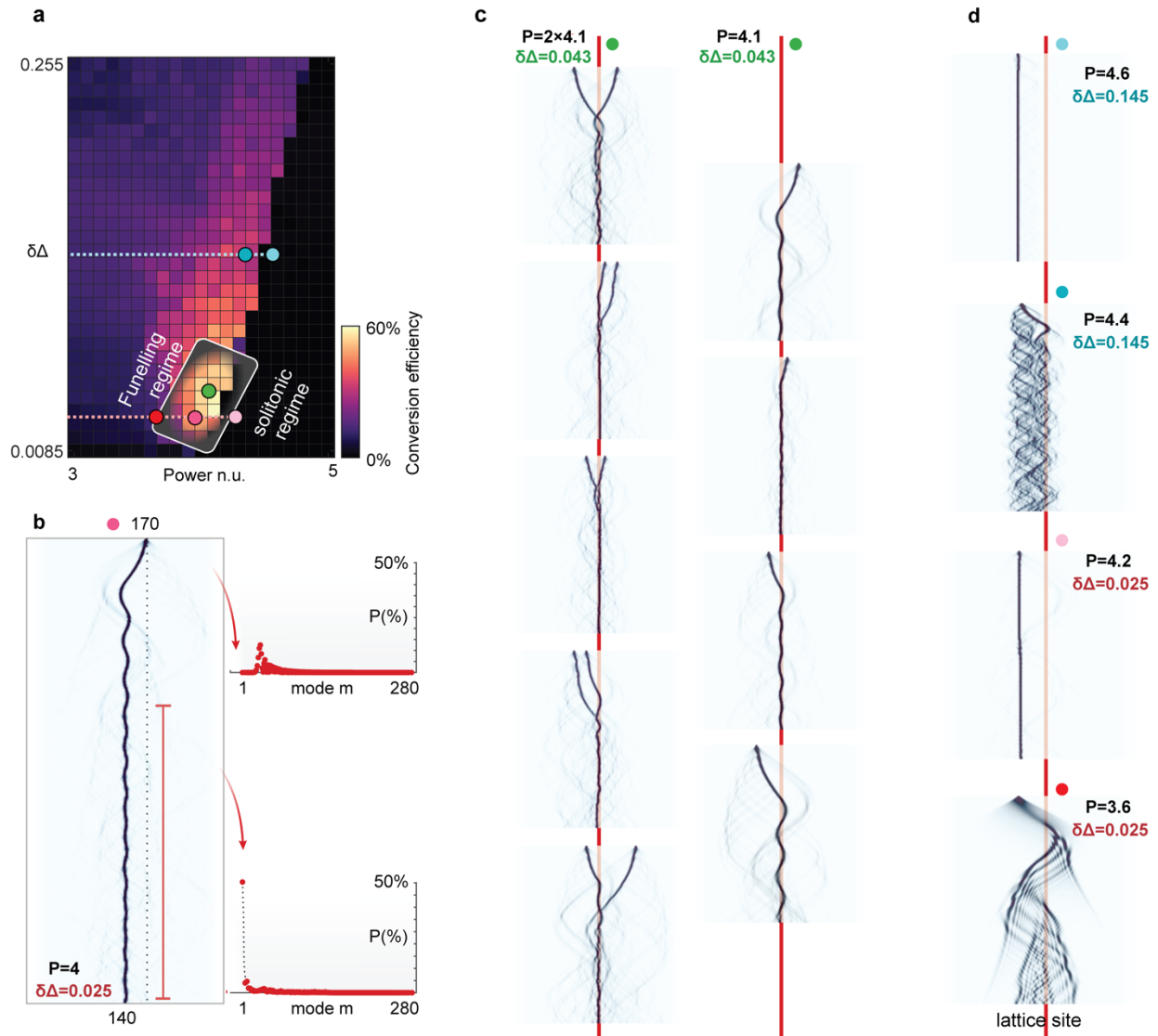


Figure S10: The effect of input power and potential slope. (a) Funneling efficiency map as a function of normalized power and detuning difference $\delta\Delta$ (representing the discrete slope of the lattice potential). The region exhibiting funneling is confined to a narrow band just before the onset of the solitonic regime. (b) The representative funneling response was observed at $P = 4$ and $\delta\Delta = 0.025$. Light is injected 30 sites away from the peak of the potential. Following funneling, power condenses into the lower-order modes, accumulating mostly within the ground state. (c) Demonstration of universal light routing behavior for single and dual injections at $P = 4.1$ and $\delta\Delta = 0.043$. (d) Examples of light dynamics beyond the funneling regime are shown at parametric points marked by colored dots in part (a). In all cases, the injection point is positioned 30 sites away from the potential peak.

Supplementary Note XI: The effect of input phase difference

To investigate the dependence of the funneling regime on the input phase difference between multiple inputs, we calculated the efficiency for the double injection case ($n = -10$ and 10) under four conditions: coherent inputs and three cases of incoherent inputs with a phase difference of $\pi/2$, $2\pi/3$, and π (Fig. S11). For this specific case, the results indicate that mutual coherence is inconsequential to the routing process. This can be directly understood given that at the final stages of funneling, light becomes thermalized close to the ground state, and as a result, the phase is no longer relevant. The field evolutions at the optimum power level and potential slope are also shown below each case. Furthermore, Fig. S11 depicts an average of 70% power concentration within the central region of the lattice over a phase difference range of 0 to 2π , further reinforcing the robustness of the funneling mechanism irrespective of input phase differences. However, in general, for a two-site input, the response can depend on the relative phase, given that interference effects could be in play, for example, by pushing the system into a solitonic regime.

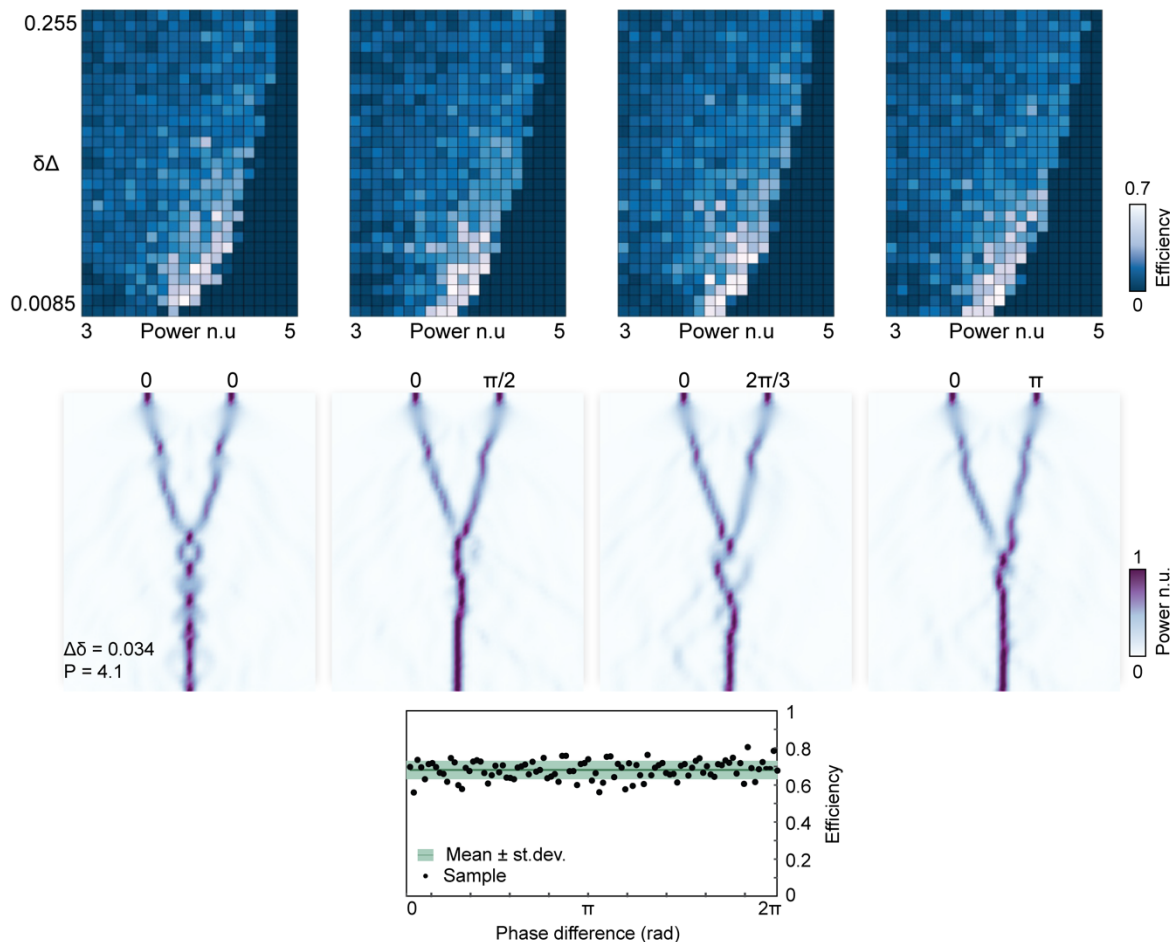


Figure S11: Investigation of the funneling regime in relation to the coherence of double injection.

Supplementary Note XII: Time-reversal symmetry

The nonlinear dynamics considered in this work are inherently Liouvillian and subject to time-reversal symmetry. To explore this property, we performed a series of numerical simulations to track the field evolution under various scenarios. Figure S12(a) shows results for both single and double injections, demonstrating a clear one-to-one mapping between input and output—evidence of the system’s time-reversal symmetric nature. In these simulations, the complex-conjugated field distribution of the funneled output is used as the input for the second part of the simulation (after step 100). However, any deviation from a perfectly phase-conjugated output is expected to result in significantly altered input conditions, due to the chaotic dynamics inherent in this complex system. Figure S12(b) illustrates how added noise at step 100 disrupts this reversibility.

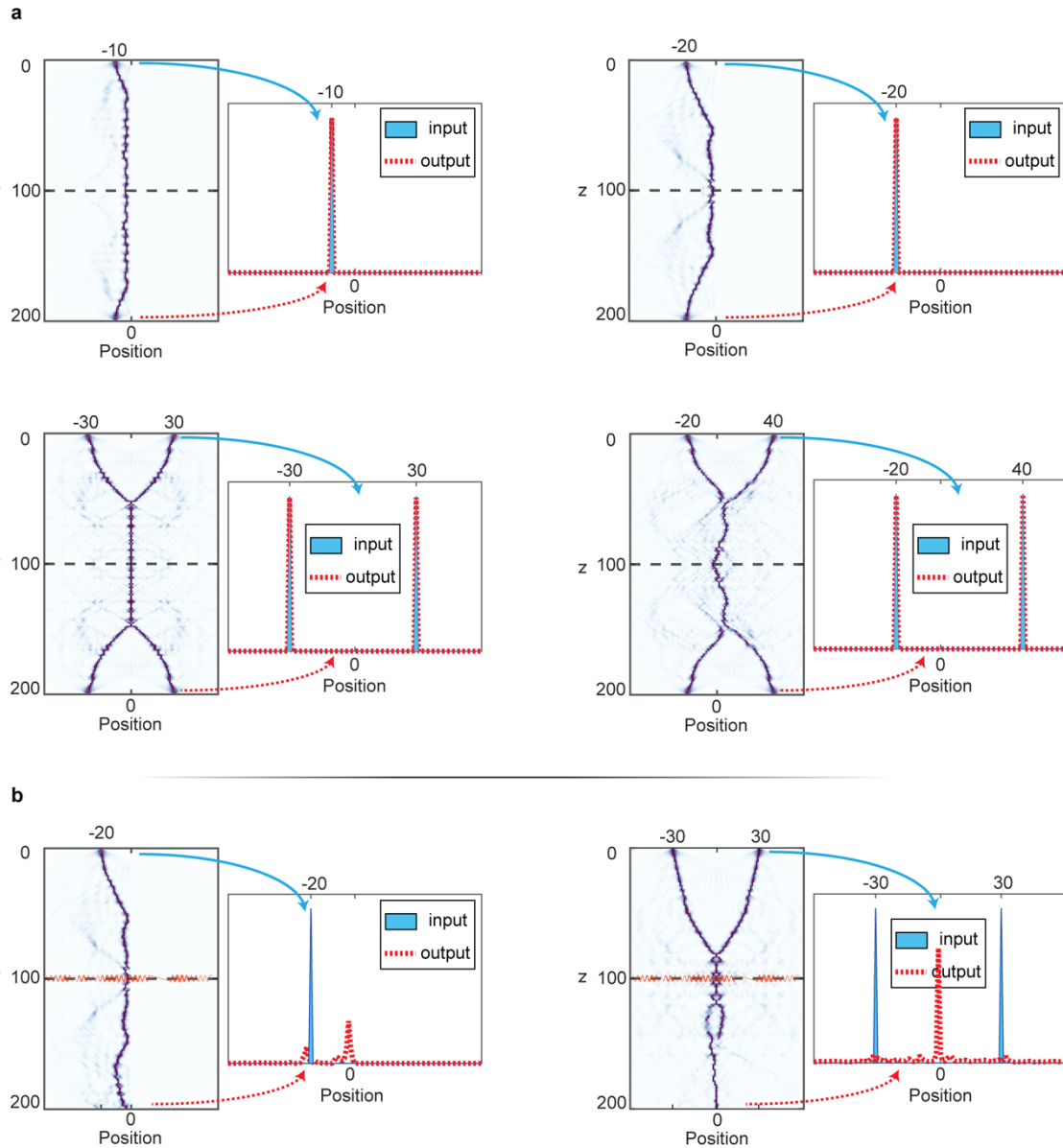


Figure S12: Time-reversal symmetry. **(a)** Simulation results of time-reversal symmetry in our system for multiple injection configurations. **(b)** The effect of the noise on the time-reversal property. The corresponding input and output intensities are denoted by blue and red dashed lines, respectively.

Supplementary Note XIII: Derivation of Thermodynamic Variables

The optical temperature of the photon gas indicates the light's tendency to concentrate in lower-order modes at positive temperatures and in higher-order modes at negative temperatures. To rigorously calculate the optical temperature and precisely predict the Rayleigh-Jeans (RJ) occupancy of the fundamental mode, it is essential to determine both the percentage of the funneled optical power P and kinetic energy U of the wavepacket following the cooling process.

A multimode nonlinear optical system thermalizes to the RJ distribution, $\langle |c_i|^2 \rangle = -\frac{T}{\epsilon_i + \mu}$. Power conservation requires that

$$\sum_i \langle |c_i|^2 \rangle = - \sum_i \frac{T}{\epsilon_i + \mu} = P \quad (\text{S10})$$

Substituting for μ from the equation of state, $U - \mu P = MT$, Eq. (S10) becomes

$$\sum_i \langle |c_i|^2 \rangle = - \sum_i \frac{T}{\epsilon_i + (U - MT)/P} = P \quad (\text{S11})$$

Given the initial condition (U, P) , Eq. (S11) can be numerically solved for T . It is important to realize that, while Eq. (S11) yields multiple solutions for T , a physically allowed solution is unique [9], and hence T is unambiguously found for a given set of (U, P) . Once T is determined, the associated μ can be derived in a straightforward manner from the equation of state.

We note that initially (during the first phase of funneling), light does not behave in a thermal manner, and the dynamics cannot be characterized by an optical temperature T . In principle, one can attempt to compute an “optical temperature” from the initial values of U and P at the input, however, the system will never thermalize at this temperature. In reality, the system begins the thermalization process only after collapsing at the peak of the potential, where a true temperature T emerges, representing an actual thermodynamic quantity. This temperature will always be significantly lower than the value computed from initial conditions.

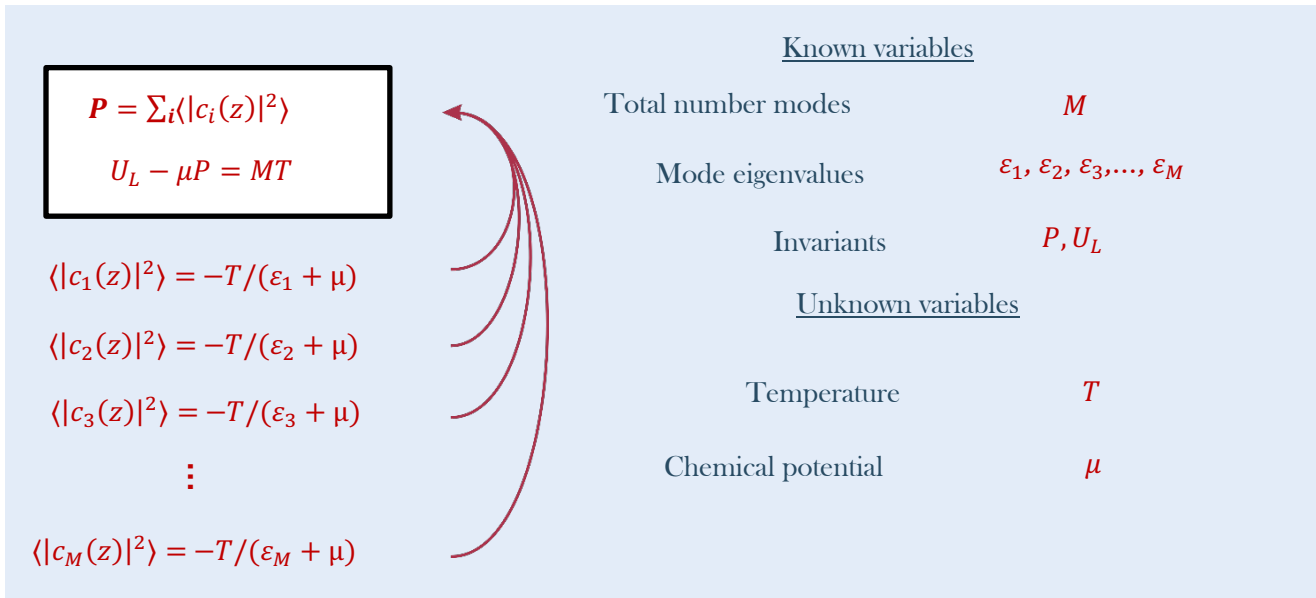


Figure S13: Thermodynamic variables. Systematic approach to derive (T, μ) from (U, P) .

Supplementary References

- [1] Grüner-Nielsen, L., Wandel, M., Kristensen, P., Jorgensen, C., Jorgensen, L.V., Edvold, B., Pálsdóttir, B., Jakobsen, D.: Dispersion-compensating fibers. *Journal of Lightwave Technology* 23(11), 3566 (2005)
- [2] Agrawal, G.P.: Nonlinear fiber optics. In: *Nonlinear Science at the Dawn of the 21st Century*, pp. 195–211. Springer, (2000)
- [3] Alberucci, A., Jisha, C.P., Monika, M., Peschel, U., Nolte, S.: Wave manipulation via delay-engineered periodic potentials. *Physical Review Research* 4(4), 043162 (2022)
- [4] Monika, M., Nosrati, F., George, A., Sciara, S., Fazili, R., Marques Muniz, A.L., Bisianov, A., Lo Franco, R., Munro, W.J., Chemnitz, M., et al.: Quantum state processing through controllable synthetic temporal photonic lattices. *Nature Photonics*, 1–6 (2024)
- [5] Pankov, A.V., Vatnik, I.D., Churkin, D.V., Sukhorukov, A.A.: Observation of localized modes at effective gauge field interface in synthetic mesh lattice. *Scientific reports* 9(1), 3464 (2019)
- [6] Miri, M.-A., Regensburger, A., Wimmer, M., Peschel, U., Christodoulides, D.N.: Solitons in optical mesh lattices. In: *Frontiers in Optics*, pp. 4–2 (2013). Optica Publishing Group
- [7] Wimmer, M., Regensburger, A., Miri, M.-A., Bersch, C., Christodoulides, D.N., Peschel, U.: Observation of optical solitons in pt-symmetric lattices. *Nature communications* 6(1), 7782 (2015)
- [8] Marques Muniz, A., Wu, F., Jung, P., Khajavikhan, M., Christodoulides, D., Peschel, U.: Observation of photon-photon thermodynamic processes under negative optical temperature conditions. *Science* 379(6636), 1019–1023 (2023)
- [9] Parto, M., Wu, F.O., Jung, P.S., Makris, K., Christodoulides, D.N.: Thermodynamic conditions governing the optical temperature and chemical potential in nonlinear highly multimoded photonic systems. *Optics Letters* 44(16), 3936–3939 (2019)